Effects of unsteady mountain-gap winds on eddies in the Red Sea

J. Farley Nicholls (1), R. Toumi (1) and G. Stenchikov (2)
(1)Space and Atmospheric Physics Group, Blackett Laboratory, Imperial College, London, U.K.
(2)Division of Physical Sciences and Engineering, King Abdullah University of Science and Technology, Saudi Arabia.
Email: james.farley-nicholls@imperial.ac.uk

November 30, 2014

Abstract

Atmosphere and ocean simulations capture the Tokar mountain-gap wind-jet and associated eddy dipole in the Red Sea. Results suggest that, once generated by a wind event, the anticyclonic eddy is further intensified through the summer by subsequent events. An asymmetry in magnitude of the two eddies is observed with the anticyclonic eddy attaining greater magnitude. A series of simulations with idealised wind forcing show that this asymmetry is not present under steady wind forcing. This effect depends on the intermittency of the wind forcing and the presence of a background northerly wind field.

1 Introduction

Mountain gap winds have been seen to induce oceanic eddy dipoles in the Gulfs of Tehuantepec, Papagayo and Panama (e.g. McCreary *et al.*, 1989; Liang *et al.*, 2009) and the Philippine Archipelago (e.g. Pullen *et al.*, 2008). The gap wind jets in the Gulf of Tehuantepec cause an eddy dipole which then propagates westward, away from the coast (Liang *et al.*, 2009). It was found (Chang *et al.*, 2012) that a subsequent wind jet can lead to an intensification of the eddy generated by the previous event. This will happen providing the interval between wind events is sufficiently small compared to the eddy propagation speed, so that the previous eddy is still in a region of enhanced wind stress curl.

A similar mountain gap wind jet and associated eddy dipole has been observed in the Red Sea (Zhai and Bower, 2013) in the region of the Tokar Gap (Figure 1a), which is located on the west side of the Red Sea, and is a 100km wide depression at around 300m elevation in the 1000m high mountains. They also noted that in the Red Sea, the eddy dipole generated by the Tokar Gap

jet will not be able to freely propagate zonally due to the eastern boundary of the basin. It therefore seems possible that these eddies might be subject to the same kind of intensification from successive wind jet events as seen in the Gulf of Tehuantepec (Chang *et al.*, 2012).

The atmospheric conditions in the region are strongly influenced by the local topography. Mountain chains run along much of the length of the Red Sea on both coastlines. This means that winds are generally constrained to flow along the axis of the Red Sea (Patzert, 1974). North-westerlies in the northern half of the basin are seen throughout the year, while in the south there is a distinct seasonality, with north-westerlies during summer and south-easterlies in winter (e.g. Pedgley, 1974; Patzert, 1974). It was noted that in winter the converging winds from the north and south funnel out of the Tokar Gap (Pedgley, 1974) while in summer winds blow through this gap onto the Red Sea (Hickey and Goudie, 2007) (see Figure 2 of Zhai and Bower, 2013 for characteristic wind fields in summer and winter). This summer wind jet through the Tokar Gap adds a cross-basin component to the wind field which would likely lead to enhanced eddy formation (Clifford *et al.*, 1997). This relationship was confirmed by (Zhai and Bower, 2013) who, using satellite altimetry and scatterometer data, found a correlation between the Tokar wind jet strength and that of an eddy dipole centered around 19^oN. The anticyclonic eddy within this dipole was also observed by ship borne ADCP measurements (Sofianos and Johns, 2007).

The formation of the eddy dipole has not previously been investigated. Satellite sea-level anomaly measurements are based on 7 day resolution data, whereas the spin-up time of the eddies has been estimated at around a day. For this reason, and given the sparsity of in-situ measurements, we take a modelling approach to investigating the impact of the Tokar Gap Jet on eddy formation. In particular we focus on how the unsteady wind forcing can affect the eddies.

2 Data and Models

2.1 Data sets

By measuring sea surface height (SSH), altimetry data can detect mesoscale eddies from their sea level anomaly. Here we use merged sea level anomaly data from AVISO (www.aviso.oceanobs.com), which combines data from the Jason-1/2, Envisat, TOPEX/Poseidan and ERS satellites. These data are provided on a 0.33^o Mercator spatial grid, and a 7-day temporal grid, and have previously been used (Zhai and Bower, 2013) to observe the eddy dipole near the Tokar Gap in 2001.

Our modelled wind fields are compared with observations from the Blended Sea Winds data set which provides daily wind speeds on a global 0.25^o grid (Zhang *et al.*, 2006). This product combines data from up to six satellites, whose measurements are taken at different points throughout the day which reduces possible temporal sub-sampling errors. Combining these different data

sources also serves to reduce the amount of missing data, and there is >75% temporal coverage of every grid cell globally.

2.2 Ocean Model

In this study we use the Regional Ocean Modeling System (ROMS) (Haidvogel *et al.*, 2000; Shchepetkin and McWilliams, 2005). The model domain is rotated clockwise at 35^o to reduce the number of land points and increase efficiency, while it encompasses the entire the Red Sea, and a portion of the Gulf of Aden which connects the Red Sea to the Indian Ocean. The model has 2 km horizontal resolution, so is able to resolve the mesoscale variability, and there are 20 vertical s-levels with increased resolution near the surface.

Initial conditions and lateral boundary forcing are taken from the Hybrid Coordinate Ocean Model (HYCOM) which is available daily at $1/12^o$ resolution (Chassignet *et al.*, 2007). The only open boundary is in the Gulf of Aden, where the Flather boundary condition is imposed for 2d momentum and radiative nudging for 3d fields. While the Red Sea is subject only to weak tides, tidal forcing is also applied at this open boundary.

ROMS has previously been used by (Liang *et al.*, 2012) to study eddy forcing mechanisms in the northeastern tropical Pacific. In that study it was found through investigating different atmospheric forcing products that the model agreed best with observations when the temporal and spatial resolution of the surface boundary conditions was increased. In order to best resolve the Tokar Gap itself, we use a regional climate model to provide surface forcing to our ocean model. Atmospheric forcing of surface energy and water fluxes and wind stress is taken from simulations of the WRF model as described in Section 2.3. Three separate, realistic, ROMS simulations are performed, from 1st June to 1st September of 2009, 2010 and 2011, the first month of each of these is used to spin-up the model before results are analysed for July and August.

A series of further simulations of ROMS is performed with idealised atmospheric forcing. Each of these has the same integrated wind forcing, but with varying degrees of intermittency. The three-day event around 3rd August 2010 is selected as a time when a strong Tokar Jet forcing is present, but winds elsewhere are comparatively weak. A steady forcing experiment is then forced with the wind-stress fields from these 3 days scaled to half their strength and repeated throughout July and August. In one intermittancy experiment this 3-day event is repeated every 6 days with 3 days of calm between events, and in two other experiments the event is scaled by 1.5 and repeated every 9 days and increased by a factor of 3 and repeated every 18 days. Each of these experiments is also forced with the shortwave radiation from 2010 and and is spun-up for June with zero winds. To isolate the effect of wind stress forcing, spatially and temporally homogeneous net surface heat and water fluxes are applied.

2.3 Atmosphere Model

We use the Advanced Research core of the Weather Research and Forecasting (ARW-WRF) model (Skamarock *et al.*, 2008) to provide atmospheric forcing to our ocean model. WRF is a fully compressible, non-hydrostatic model which uses a terrain-following coordinate system. Our model is run on two one-way nested grids of 30 and 10 km resolution, with the inner grid centered on the Red Sea region and completely encompassing the ocean model grid. This 10 km resolution is sufficient to accurately represent the Tokar Gap and the wind jet through it (e.g. Jiang *et al.*, 2009). Initial and boundary conditions are taken from the 6 hourly reanalysis fields of ERA-Interim (Dee *et al.*, 2011). The boundary conditions are applied over a buffer zone of five grid cells and there is no nudging within the interior of the grid. Three WRF simulations are performed for the summer seasons of 2009-2011, each running from 1st June to 1st September. The output, including net surface heat and water fluxes, short wave radiation and wind-stress components is used to force the ocean model at 3 hour intervals.

3 Results

The July and August mean wind speed field from the Sea Winds observations over the three years of simulation is shown in Figure 1b. The effect of the Tokar Gap is clearly seen in a band of strong winds emerging from the gap and then showing signs of being advected southward. This is compared to the WRF simulation results (Figure 1a) which also demonstrate strong winds in the Tokar Gap region curving southward with the prevailing along-basin winds. There is good qualitative agreement between simulated and observed wind speeds, with the areas of intense and calm winds showing good consistency. As expected, our mean wind fields are also in close agreement with those seen in the WRF simulations of (Jiang *et al.*, 2009) whose model compared well with in-situ measurements.

The model consistently shows stronger anticyclonic than cyclonic eddies. Figure 1d shows the mean SSH anomaly from July and August 2009-2011 in the AVISO satellite data. A number of eddies are apparent: there is a string of positive and negative SSH anomalies at around 24, 23, 22, 20 and 18^{o}N, with the positive features clearer than the negative and the largest of these located at around 24^{o}N. The eddies at 18 and 20^{o}N were previously seen in other years of the AVISO data by (Zhai and Bower, 2013) and are associated with the Tokar Jet. The negative feature near 20^{o}N curves southward around the positive anomaly just south of it, and is caused by the southward curving of the wind jet. These observations can be qualitatively compared with ROMS results in Figure 1c. In Figure 1c there is a very strong negative feature northward of 25^{o}N, which is not seen in the AVISO data. This cyclonic eddy was observed in (Sofianos and Johns, 2007) as a year-round feature, and so would not show up in Figure 1d which is an anomaly field. In ROMS the same string of positive

and negative SSH features between 21-24^{o}N as AVISO is noted, although shifted slightly southwards in the simulations. The positive anomaly at 18-19^{o}N caused by the Tokar Jet is very strong in ROMS, however the negative anomaly is not evident here. The cyclonic eddy can be seen in the individual years of data (not shown), however as it is weaker than the anticyclonic eddy and the eddy location varies temporally (seen in the next section) this is washed out in the 3 year average SSH shown in Figure 1c. The eddies throughout the central and southern Red Sea compare well between AVISO observations and ROMS simulations, in particular the presence of an eddy caused by Tokar Jet forcing is noted in each.

We now examine the Tokar Jet strength and its relation with the ocean eddies. We define a box near the jet exit, as shown in Figure 1a, where we calculate the absolute magnitude of the wind stress curl at each point, and take a mean across the box. This metric is used as a measure of the strength of the Tokar Jet. In each year there are no jet events in June and they are concentrated in July and August (Figures 2a,c,e). Our model results also demonstrate the strong diurnal cycle, caused by the land-sea breeze, seen in the model results of (Jiang *et al.*, 2009) and the observations of (Zhai and Bower, 2013) although we remove this from the results shown in Figure 2.

By the end of August in each year there is an eddy dipole present, with a positive sea-surface height around 19^{o}N and a negative height north of this (Figures 2b,d,f). There is however some variation in the location of the eddies, with those in 2010 further south than 2009, and a northward progression during August 2011. This shift in location is largely responsible for the missing negative SSH in the 3-year mean in Figure 1d as at 20^{o}N there is a strong negative feature in 2009, but positive throughout 2010, and then positive in July 2011 and negative in August 2011. In each year it is also clear that the eddy structure is not present in the initial conditions and throughout June. In 2009 (Figure 2b) the eddies are initiated after the Tokar Jet event of 3rd July and then the magnitude of the anticyclone is increased by the event starting around July 16th while the cyclone intensity decreases, after which the magnitude of the dipole remains largely unchanged until the end of the simulation. During 2010 the eddies do not appear until later as there are no wind events until July 13th. After that point the anticyclonic eddy is intensified by a series of wind events on July 18th and 23rd, then another series of events starting on August 3rd regenerate the eddy slightly further south. In 2011 the eddy dipole emerges in a weak state around mid-June, although there is no obvious wind jet forcing event for this. In July however the anticyclonic eddy becomes much stronger, again driven by a series of Tokar Jet events particularly the ones on July 17th, 30th July and August 3rd. A clear tendency emerges throughout these simulations that the anticyclonic eddy tends to be stronger than the cyclonic eddy.

Figure 3 shows the cross-basin currents against depth. The anticyclonic eddy can be identified here as the positive across-basin velocities just north of 19^{o}N and negative velocities south of this, while the cyclonic eddy involves the same positive velocities and the negative velocities around 20^{o}N. The anticyclonic eddy is stronger than the cyclonic eddy as was apparent in Figure 2. The

core of both eddies is confined to the top 40 m of the water column, but the anticyclonic eddy in particular extends to between 200-250 m, which is deeper than the previous observation. At most other points during the simulations the depth of the anticyclonic eddy was between 100-150 m which agrees with the observation (Sofianos and Johns, 2007), but suggests that the eddy can get significantly deeper than this.

From the realistic model simulations, the overall picture is that there is an asymmetry in the eddy dipole, which is initially generated by Tokar Jet forcing and that once the anticyclonic eddy forms it is intensified by subsequent wind jet events. This is further investigated in a series of experiments with idealised atmospheric forcing (described in Section 2.2), where each simulation has the same integrated wind forcing, but with varying degrees of intermittency.

Along axis slices of the SSH for each of these idealised experiments are shown in Figure 4. In Figure 4a where the steady forcing is applied, the eddy dipole appears during early July, as expected, and continues to strengthen throughout the two months of forcing. In this case both the cyclonic and anticyclonic eddies seem to act similarly. When the forcing is doubled but applied only half of the time (Figure 4b), the eddies also begin to appear in early July and then increase in magnitude intermittently with each subsequent wind event. The magnitude of the positive SSH anomaly is however greater both than the negative anomaly and also than when the steady forcing is applied. The opposite is true of the cyclonic eddy, which seems not to further strengthen after the first month and which is therefore weaker than under steady forcing. There is a similar picture when the intermittency of the forcing is increased further (Figures 4c,d) of stronger positive SSH, and weaker negative SSH than with steady forcing. From Figure 4d it can clearly be seen that the cyclonic eddy is at its strongest at the time when the wind forcing is applied and weakens thereafter, whereas, the anticyclonic eddy weakens at the onset of forcing before strengthening when the forcing is removed. It is therefore clear that the intermittency of the wind jet forcing is the cause of the asymmetry in the eddy dipole response, and that this asymmetry comes both in timing and intensity of the eddies.

4 Discussion

By performing realistic atmospheric and oceanic simulations of the Red Sea during summer months we were able to replicate the observed mountain gap wind jet, and associated eddy dipole near the Tokar Gap. The mechanism for the formation of this eddy dipole is believed to be the Ekman pumping caused by a positive wind stress curl to the left of the wind jet, and negative curl to the right. This results in a cyclonic eddy with a negative sea level anomaly to the left of the jet, and an anticyclonic eddy and positive sea level anomaly to its right. Given the 3-dimensional nature of the simulations, we were able to find that while the anticyclonic eddy caused by the Tokar Jet generally extends to 100-150 m depth as in the only existing measurement (Sofianos and Johns, 2007), the eddy can reach deeper than this, to around 250 m.

The eddies can be intensified by subsequent Tokar Jet events as seen by (Chang *et al.*, 2012) in the north-eastern tropical Pacific. It was also noted that there was an asymmetry in the eddy dipole, with a stronger anticyclone than cyclone. It was found that under steady wind jet forcing there is no asymmetry in the eddy behaviour. However under oscillatory forcing, the anticyclonic eddy is stronger than with steady forcing and the cyclonic eddy is weaker. There is also observed to be an asymmetry in the timing of the onset of the eddies, with the cyclone appearing immediately with the forcing, but the anticyclone appearing behind the wind jet.

What causes this asymmetric response between the cyclonic and anticyclonic eddies is less clear. For a wind jet without background flow, there will be no turning of the wind stress at a fixed ocean grid point (Figure 5a). However given that the climatology of the surface wind field in the Red Sea is for northerly winds, the picture is different. Before a jet event the winds are northerly, during the event they veer westerly, and then when the event dies out they return to northerlies. This means that at a fixed point in the path of the jet, winds veer cyclonically as the jet approaches and then anticyclonically as it passes (Figure 5b). This leads to a directly wind-driven enhancement of the, Ekman forced, cyclonic eddy as the jet approaches, and an enhancement of the anticyclonic eddy behind it. This asymmetry in timing can explain the idealised simulations with unsteady forcing. If this mechanism is present then it would imply that the asymmetry is caused by the intermittency of the wind forcing, which would explain why it was not seen in the idealised simulations of (Zhai and Bower, 2013) who applied steady Tokar Gap wind forcing.

5 Conclusions

Our realistic atmosphere and ocean simulations of the Red Sea captured the observed summer-time Tokar Gap wind-jet and associated eddy dipole. It was found that throughout the summer the magnitude of the anticyclonic eddy was increased by each wind event. It was also noted that the anticyclonic eddy was generally stronger than the cyclonic eddy. Experiments with idealised wind forcing confirmed this result when the forcing was intermittent. Under steady forcing the two eddies were symmetric. Another asymmetry between the two eddies was in timing: the cyclonic eddy appears at the onset of wind forcing and the anticyclonic eddy after it. It is reasoned that this effect is caused by a cyclonic veering of the wind stress from its background northerly direction to westerlies as the event begins, and then an anticyclonic veering back to northerlies as the jet passes. This veering could enhance the respective eddies, and result in this asymmetry in timing.

6 Acknowledgments

We would like to thank King Abdullah University of Science and Technology (KAUST) and the BP Environmental Technology program for funding this research.

References

C.-H. Chang, S.-P. Xie, N. Schneider, B. Qiu, J. Small, W. Zhuang, B. Taguchi, H. Sasaki, and X. Lin. East Pacific ocean eddies and their relationship to subseasonal variability in Central American wind jets. *Journal of Geophysical Research: Oceans (1978–2012)*, 117(C10), 2012.

E. P. Chassignet, H. E. Hurlburt, O. M. Smedstad, G. R. Halliwell, P. J. Hogan, A. J. Wallcraft, R. Baraille, and R. Bleck. The HYCOM (hybrid coordinate ocean model) data assimilative system. *Journal of Marine Systems*, 65(1):60–83, 2007.

M. Clifford, C. Horton, J. Schmitz, and L. H. Kantha. An oceanographic nowcast/forecast system for the Red Sea. *Journal of Geophysical Research: Oceans (1978–2012)*, 102(C11):25101–25122, 1997.

D. Dee, S. Uppala, A. Simmons, P. Berrisford, P. Poli, S. Kobayashi, U. Andrae, M. Balmaseda, G. Balsamo, P. Bauer, et al. The ERA-Interim reanalysis: Configuration and performance of the data assimilation system. *Quarterly Journal of the Royal Meteorological Society*, 137(656):553–597, 2011.

D. Haidvogel, H. Arango, K. Hedstrom, A. Beckmann, P. Malanotte-Rizzoli, and A. Shchepetkin. Model evaluation experiments in the North Atlantic Basin: simulations in nonlinear terrain-following coordinates. *Dynamics of Atmospheres and Oceans*, 32(3-4):239–281, 2000.

B. Hickey and A. Goudie. The use of TOMS and MODIS to identify dust storm source areas: The Tokar delta (Sudan) and the Seistan basin (south west Asia). *Geomorphological variations*, pages 37–57, 2007.

H. Jiang, J. T. Farrar, R. C. Beardsley, R. Chen, and C. Chen. Zonal surface wind jets across the Red Sea due to mountain gap forcing along both sides of the Red Sea. *Geophysical Research Letters*, 36(19), 2009.

J.-H. Liang, J. C. McWilliams, and N. Gruber. High-frequency response of the ocean to mountain gap winds in the northeastern tropical Pacific. *Journal of Geophysical Research: Oceans (1978–2012)*, 114(C12), 2009.

J.-H. Liang, J. C. McWilliams, J. Kurian, F. Colas, P. Wang, and Y. Uchiyama. Mesoscale variability in the northeastern tropical Pacific: Forcing mechanisms and eddy properties. *Journal of Geophysical Research: Oceans (1978–2012)*, 117(C7), 2012.

J. P. McCreary, H. S. Lee, and D. B. Enfield. The response of the coastal ocean to strong offshore winds: With application to circulations in the Gulfs of Tehuantepec and Papagayo. *Journal of Marine Research*, 47(1):81–109, 1989.

W. C. Patzert. Wind-induced reversal in Red Sea circulation. In *Deep Sea Research and Oceanographic Abstracts*, volume 21, pages 109–121. Elsevier, 1974.

D. Pedgley. An outline of the weather and climate of the Red Sea. *Loceanographie physique de la Mer Rouge*, pages 9–27, 1974.

J. Pullen, J. D. Doyle, P. May, C. Chavanne, P. Flament, and R. A. Arnone. Monsoon surges trigger oceanic eddy formation and propagation in the lee of the Philippine Islands. *Geophysical Research Letters*, 35(7), 2008.

A. Shchepetkin and J. McWilliams. The regional oceanic modeling system (ROMS): a split-explicit, free-surface, topography-following-coordinate oceanic model. *Ocean Modelling*, 9(4):347–404, 2005.

W. Skamarock, J. Klemp, J. Dudhia, D. Gill, D. Barker, W. Wang, and J. Powers. *A description of the Advanced Research WRF Version 2*. Citeseer, 2005.

S. S. Sofianos and W. E. Johns. Observations of the summer Red Sea circulation. *Journal of Geophysical Research: Oceans (1978–2012)*, 112(C6), 2007.

P. Zhai and A. Bower. The response of the Red Sea to a strong wind jet near the Tokar Gap in summer. *Journal of Geophysical Research: Oceans*, 118(1):421–434, 2013.

H.-M. Zhang, J. J. Bates, and R. W. Reynolds. Assessment of composite global sampling: Sea surface wind speed. *Geophysical Research Letters*, 33(17), 2006.

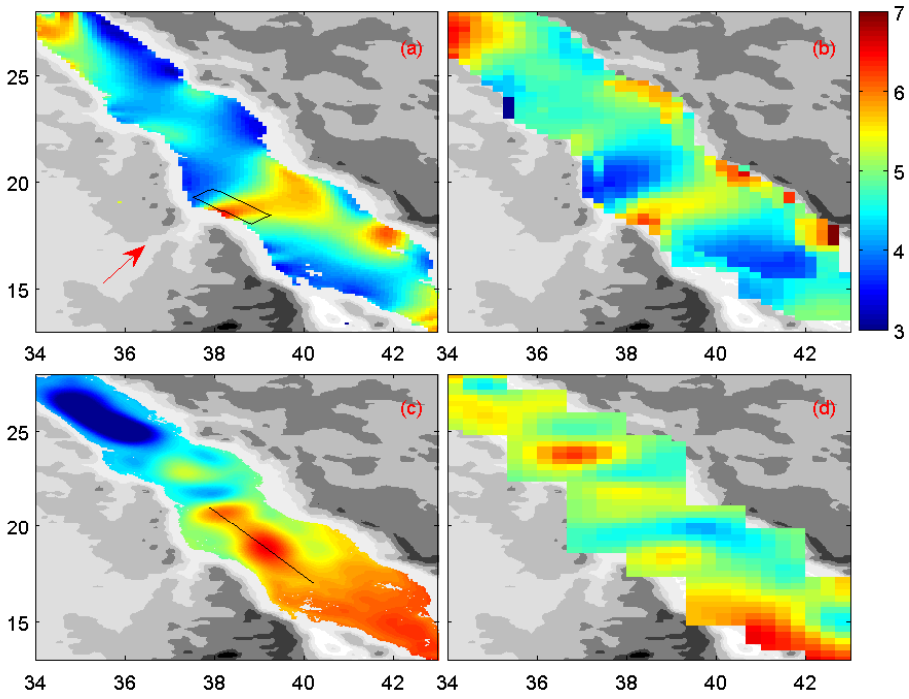

Figure 1: (top) Mean July and August wind speeds (m/s) for 2009-2011 from (a) WRF simulations, (b) Sea Winds satellite measurements. (bottom) July and August mean from 2009-2011 for (c) sea-surface height from ROMS simulations, (d) mean sea-level anomaly from AVISO data. Topography is shown in the gray scale, with shading intervals of <0m, 0-250, 250-500, 500-1000, 1000-2000, 2000-3000m.

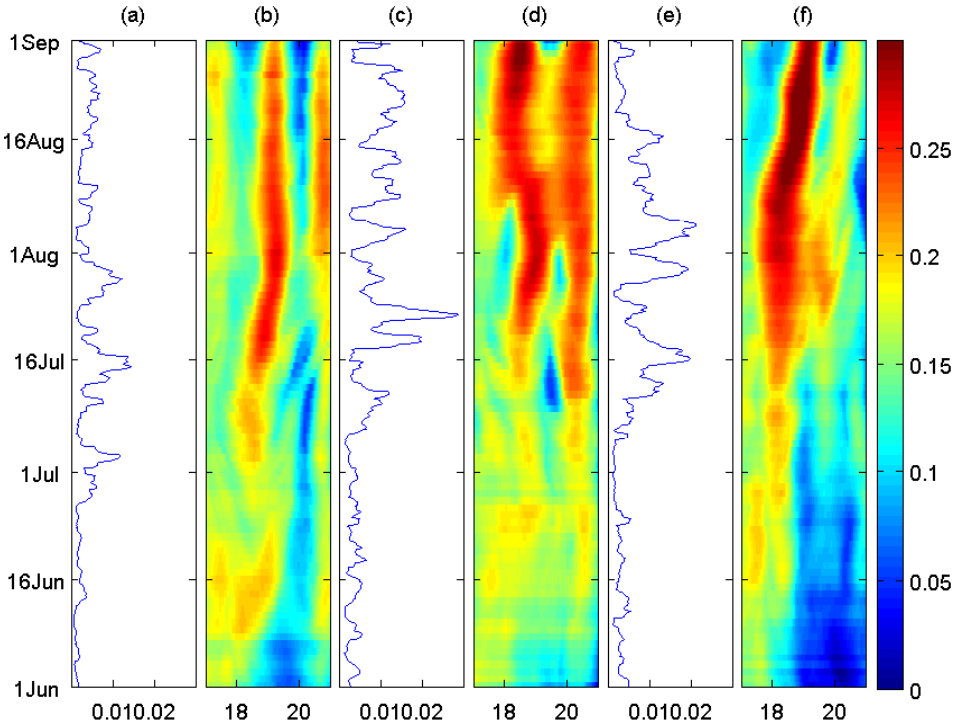

Figure 2: Mean absolute wind stress curl (N/m^3) in the box indicated in Figure 1b for (a) 2009, (c) 2010, (e) 2011 from WRF simulations. Temporal evolution of sea-surface height (m), on an along axis cross-section, from ROMS simulations for (b) 2009, (d) 2010, (f) 2011 where the x-axis displays the latitude along the basin-section.

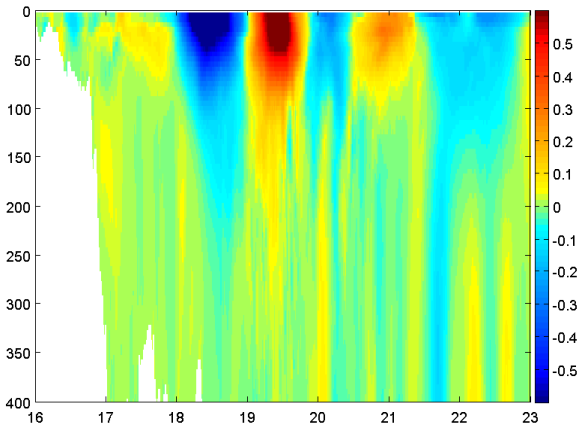

Figure 3: Along-axis cross-section of across-basin currents (m/s) from 24th August 2011 plotted against depth (m), with latitude on the x-axis.

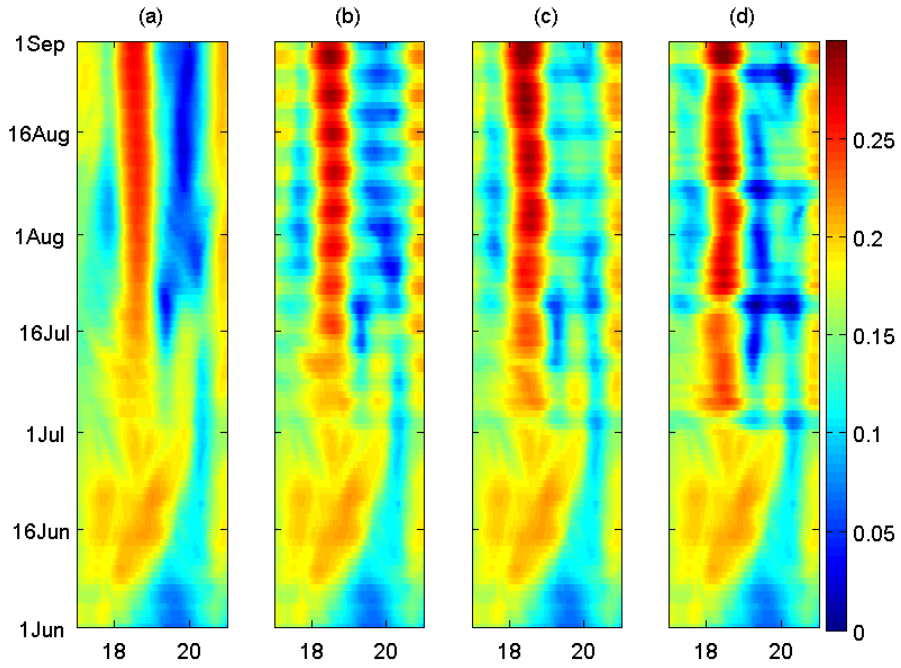

Figure 4: Temporal evolution of sea-surface height (m), on an along axis cross-section, from idealised ROMS simulations. (a) Steady Tokar Gap forcing, (b) double strength forcing applied 3 days on 3 days off, (c) 3 times the forcing applied 3 days on 6 days off, (d) 6 times forcing applied 3 days on 15 days off.

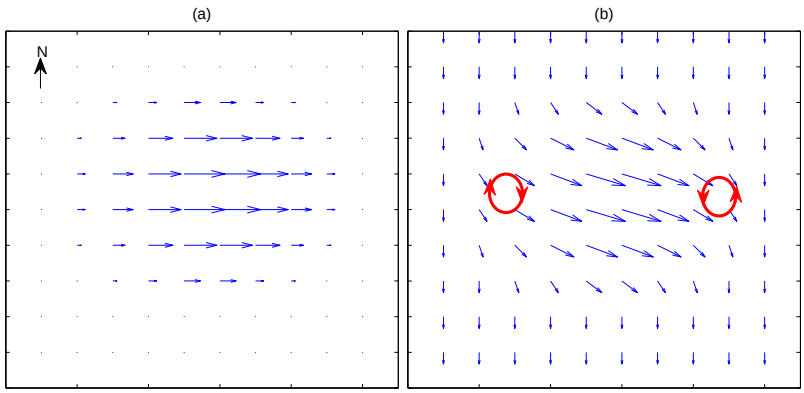

Figure 5: Schematic of (a) westerly wind-jet, (b) westerly wind-jet with background northerly wind field. Viewed from a fixed point on the sea, the wind stress veers cyclonically at the onset of the jet and anticyclonically behind it when there is this northerly background wind field, as indicated by the red arrows.